Effective implementation of numerical models for the crashworthiness of composite laminates

M.P. Falaschetti [*], F. Rondina, N. Zavatta, E. Troiani, L. Donati

University of Bologna, Department of Industrial Engineering, Via Fontanelle 40, 47121 Forlì, FC, Italy

A B S T R A C T

Crashworthiness is the capability to leverage the controlled failure of a structure to dissipate the kinetic energy of an impact, thus protecting occupants of vehicles and valuable equipment. Composite materials have exciting potential in airborne and ground vehicles' crashworthy structures thanks to their high Specific Energy Absorption. However, their performances depend on several design factors, such as material constituents, stacking sequence, and component geometry. Numerical simulations have proved to be a valid tool to analyze the effect of these parameters and streamline the design phase, reducing costs and time to market. Nevertheless, material calibration is a critical step in implementing reliable numerical simulations. ESI Virtual Performance Solution software supports two damage models for orthotropic laminae: Ladevèze and Waas-Pineda. After a brief description of the two models, the required calibration procedures for a unidirectional ply laminate are presented.

1. Introduction

In aeronautical and automotive vehicles, crash-absorbing structures ensure the safety of occupants and payload. Composite materials have shown high performances [1,2] and, therefore, are widely used in energy-absorbing structures [3]. However, crashworthiness properties are influenced by several design factors such as composite constituents [4–6], trigger [7], profile geometry [8], working environment [9,10], etc. Experimental studies of the influence of each parameter would lead to costly and time-consuming campaigns. For this reason, different numerical models and modeling strategies have been developed to simulate the crushing event at different dimensional scales and detail levels. Large structures are usually modeled with simplified approaches, losing predictive capabilities but gaining the possibility to evaluate the responses of multiple structures in a short time. More detailed simulations allow an in-depth analysis of the physics of crushing but require higher computational time and longer preprocessing phases. The choice of damage models is influenced by the final aim of the numerical analysis: Progressive Failure Models (PFM [11,12]) are usually implemented in large-scale simulations, giving, however, no chance to analyze the crushing morphology and complexity; Continuum Damage Models (CDM [13,14]) implement damage parameters to evaluate the material damage evolution and the material degradation throughout the crushing event; Non-local Damage Models (NDM [15,16]) have the versatility of the previous models while overcoming the characteristic mesh sensitivity of CDMs. The last two models are nowadays widely used for crashworthiness simulations; still, they both require the identification of several material constitutive and modeling parameters to be obtained following software user-manuals guidelines. However, manuals are usually brief, contain many references to regulations and papers, and often

* Corresponding author at: Department of Industrial Engineering (DIN), University of Bologna, via Fontanelle 40, 47122 Forlì, FC, Italy.
E-mail address: mariapi.falaschetti2@unibo.it (M.P. Falaschetti).

offer little in terms of operative procedures. Focusing on Unidirectional (UD) composite laminates, this paper aims to provide the reader with a short guide containing a brief theoretical description and a more extensive practical procedure for the implementation and calibration of Ladevèze CDM model [13,17] and Waas-Pineda NDM model [18,19] in ESI-VPS Visual-Crash PAM v18.0-2022 software.

2. Models description

Different failure modes can be identified in compressive crush events of composite structures. The most important are fiber fragmentation, splaying of lamina bundles, and wall buckling, each of which is associated with different energy dissipations [8,20]. Numerical simulations, therefore, should consider these failure modes correctly to ensure reliable results. Moreover, due to the layered nature of a composite component, the delamination failure mode must also be modeled accurately. Consequently, a composite structure is commonly modeled employing different shell layers, representing a single ply or bundles of aligned plies each, and interactions between them to simulate interlaminar behavior.

The following sections provide an in-depth look at the ESI-VPS shell modeling, strictly related to unidirectional composite plies.

2.1. Basic shell model

In this work, the composite laminates are modeled by means of plate shell elements, where the properties of the unidirectional fiber-reinforced material are homogenized. This results in a transversely isotropic lamina that could be defined by six parameters: two Young's moduli in the longitudinal and transverse direction, the Poisson's modulus, and three shear moduli. Conventionally, for unidirectional composites, G_{13} is considered equal to G_{12} and, therefore, the stiffness tensor can be defined as in (1).

$$\begin{pmatrix} \varepsilon_{11} \\ \varepsilon_{22} \\ \varepsilon_{23} \\ \varepsilon_{13} \\ \varepsilon_{12} \end{pmatrix} = \begin{Bmatrix} \frac{1}{E_{11}} & -\frac{\nu_{12}}{E_{11}} & 0 & 0 & 0 \\ -\frac{\nu_{12}}{E_{11}} & \frac{1}{E_{22}} & 0 & 0 & 0 \\ 0 & 0 & \frac{1}{2G_{23}} & 0 & 0 \\ 0 & 0 & 0 & \frac{1}{2G_{13}} & 0 \\ 0 & 0 & 0 & 0 & \frac{1}{2G_{12}} \end{Bmatrix} \begin{pmatrix} \sigma_{11} \\ \sigma_{22} \\ \sigma_{23} \\ \sigma_{13} \\ \sigma_{12} \end{pmatrix} \tag{1}$$

where ε_{ij} represent the strains, σ_{ij} the stresses, E_{ij} the Young's moduli, G_{ij} the shear moduli, and ν_{12} the Poisson's modulus. The subscripts i and j can be equal to 1, 2, or 3, representing the plane on which the property is calculated.

The damage is modeled throughout the degradation of the material stiffness as $E_{ij}^d = \left(1 - d_{ij}\right)E_{ij}^0$, where d_{ij} is the damage parameter, varying from 0 (undamaged conditions) to 1 (ultimate failure). The superscript 0 or d refers to the as-built and damaged quantities, respectively. When the material has totally failed, i.e. $d_{ij} = 1$, the stiffness is null, resulting in the inability to transfer the load.

2.2. Ladevèze model

The Ladevèze (LV) model [19,20] represents the composite material's global response starting from the individual lamina's local deformation status. The scalar damage parameters affecting the constitutive equations are non-interactive and non-healing. This means that damage values for different loading conditions are independent, and their value cannot decrease during loading. Moreover, the in-plane shear moduli are the only ones affected by the damage evolution.

The *fiber damage* is based on linear moduli reduction between two limit strains, followed by a region where the stress is bounded above. Under compression loads, fibers are subjected to micro-buckling that leads to a nonlinear behavior in the fiber direction; therefore, a softening parameter γ is introduced, as shown in (2).

$$E_{11}^d = \begin{cases} \left(1 - d_{ij}\right)E_{11t}^0 & \text{tension} \\ \left(1 - d_{ij}\right)\dfrac{E_{11}^{0c}}{1 + \gamma E_{11}^{0c}|\varepsilon_{11}|} & \text{compression} \end{cases} \tag{2}$$

with

$$\gamma = \frac{E_{11}^{0c} - E_{11}^{\gamma}}{E_{11}^{\gamma} E_{11}^{0c} |\varepsilon_{11}^{\gamma}|} \tag{3}$$

where E_{11}^{0c} is the elastic modulus in the initial loading step, E_{11}^{γ} the tangent elastic modulus in the non-linear stage, and $\varepsilon_{11}^{\gamma}$ the related deformation (Fig. 1).

The *matrix damage* model derives from two physical phenomena: the debonding between fibers and matrix, and the micro-cracking of the matrix parallel to the fiber direction. The damage evolution functions, Y_s and Y_t, considering these two phenomena, are defined as

$$Y_s = \sqrt{Z_s + bZ_t}$$

$$Y_t = \sqrt{Z_t} \tag{4}$$

where Z_s and Z_t are the damage functions for the shear and transverse directions respectively, b is an optional coupling factor between shear and transverse direction, which is unused in this work. The damage functions are calculated as:

$$Z_i = \frac{\partial E_D}{\partial d_i} \tag{5}$$

with E_D representing the strain energy density $E_D = \int_0^{\varepsilon_i} \sigma_i d\varepsilon_i$, where σ_i is the stress and ε_i the strain, and d_i the scalar damage parameter in shear or transverse conditions.

Finally, the *matrix plasticity* is implemented using a hardening law depending on the effective plastic strain p, as $R(p) = R_0 + \beta(p)^m$, where the initial yield stress R_0 and the hardening parameters β and m are determined experimentally.

Failed elements are removed from the simulation by means of the *element elimination* settings that can be defined in two different modalities: through an equivalent shear strain limit (which cannot be triggered by normal loading modes but is only activated by shear deformation) or a more detailed strain-based failure method (allowing the definition of strain limits in three axial and three shear directions, both positive and negative).

2.3. Waas-Pineda model (WP)

The Waas-Pineda model [18,19,21] implemented in the ESI-VPS software inherits the orthotropic elasticity and matrix plasticity from Ladevèze and adds a nonlocal crack formulation to allow material softening effectively. The material behavior throughout the loading is modeled by means of three distinct states characterized by irreversible transitions (Fig. 2): continuum, cohesive, and post-damage states. The continuum state represents the pristine material condition up to the first damage occurrence; in the cohesive state, the damage propagates up to a maximum damage value, while in the last stage, it remains constant. The transition from the continuum to the cohesive state is triggered by a quadratic failure criterion. In contrast, the second transition, from cohesive to post-damage state, follows a maximum allowable damage criterion.

The quadratic failure criterion can be stress-based or strain-based as shown in (6):

$$\left(\frac{\sigma_{11}}{\Sigma_{11,t}}\right)^2 \geq 1 \ , \ \left(\frac{\varepsilon_{11}}{E_{11,t}}\right)^2 \geq 1 \ \ if \ \sigma_{11} > 0 \ or \ \varepsilon_{11} > 0 \tag{6}$$

$$\left(\frac{\sigma_{11}}{\Sigma_{11,c}}\right)^2 \geq 1 \ , \ \left(\frac{\varepsilon_{11}}{E_{11,c}}\right)^2 \geq 1 \ \ if \ \ \sigma_{11} < 0 \ \ or \ \ \varepsilon_{11} < 0$$

$$\left(\frac{\sigma_{22}}{\Sigma_{22,t}}\right)^2 + \left(\frac{\sigma_{12}}{T_{12}}\right)^2 \geq 1 \ , \ \left(\frac{\varepsilon_{22}}{E_{22,t}}\right)^2 + \left(\frac{\varepsilon_{12}}{\Gamma_{12}}\right)^2 \geq 1 \ if \ \sigma_{22} > 0 \ or \ \varepsilon_{22} > 0$$

$$\left(\frac{\sigma_{22}}{\Sigma_{22,c}}\right)^2 + \left(\frac{\sigma_{12}}{T_{12}}\right)^2 \geq 1 \ , \ \left(\frac{\varepsilon_{22}}{E_{22,c}}\right)^2 + \left(\frac{\varepsilon_{12}}{\Gamma_{12}}\right)^2 \geq 1 \ if \ \sigma_{22} < 0 \ or \ \varepsilon_{22} < 0$$
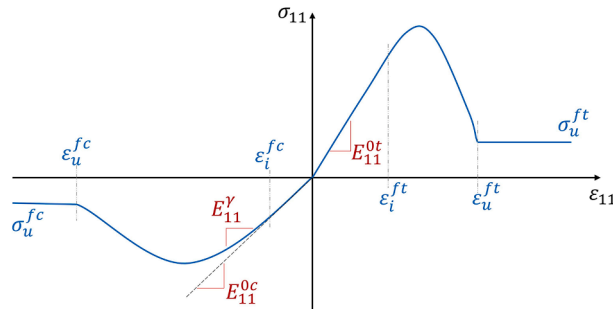

Fig. 1. Fiber direction tension and compression material behavior. The represented parameters are: E_{11}^γ, the tangent elastic modulus in the non-linear stage for compression loading; E_{11}^{0j}, the elastic modulus in the undamaged step; ε_i^{fj}, the strain at the first non-linearity; ε_f^{fj}, the strain at the damage end; σ_u^{fj}, the ultimate failure stress. $j = c \ or \ t$, for compression or tension loading conditions, respectively.
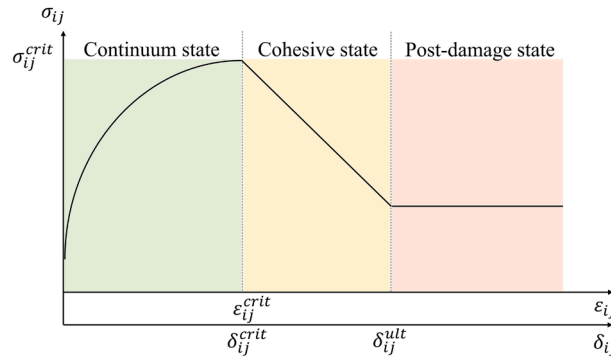
Fig. 2. Example of the three distinct states of the Waas-Pineda damage model.

where considering $j = c, t$ for tensile and compressive property respectively, Σ_{11j} is the longitudinal initiation stress, Σ_{22j} is the transversal initiation stress, T_{12} is the in-plane shear initiation stress, E_{11j} is the longitudinal initiation strain, E_{22j} is the transversal initiation strain, Γ_{12} is the in-plane shear initiation strain, σ_{11} is the longitudinal stress, σ_{22} is the transversal stress, σ_{12} is the shear stress, ε_{11} is the longitudinal strain, ε_{22} is the transversal strain, ε_{12} is the shear strain.

The *cohesive state* uses traditional bilinear cohesive traction-separation $\sigma(\delta)$ laws and is characterized by cohesive stiffness $K = \sigma/\delta$ and parameters for fiber and matrix damage. Considering the longitudinal, transverse, and shear loads, the traction-separation laws can be conveyed as in (7):

$$\begin{aligned}
\sigma_{11} &= (1 - D_f)K_{11}\delta_{11} \\
\sigma_{22} &= (1 - D_m)K_{22}\delta_{22} \\
\sigma_{12} &= (1 - D_m)K_{12}\delta_{12}
\end{aligned} \tag{7}$$

where the fiber and matrix damage parameters are defined as:

$$D_f = \frac{\delta_{11}^{ult}\left(\delta_{11} - \delta_{11}^{crit}\right)}{\delta_{11}\left(\delta_{11}^{ult} - \delta_{11}^{crit}\right)} \quad , \quad D_m = \frac{\delta_m^{ult}\left(\delta_m - \delta_m^{crit}\right)}{\delta_m\left(\delta_m^{ult} - \delta_m^{crit}\right)} \tag{8}$$

and the ultimate separation derives from the critical fracture energies G_{Ckk} in longitudinal ($k = 1$) and transversal ($k = 2$) direction:

$$\delta_{11}^{ult} = \frac{2G_{C11}}{\sigma_{11}^{crit}} \tag{9}$$

$$\delta_{22}^{ult} = \frac{2G_{C22}}{\sigma_{22}^{crit}}$$

The matrix-dominated damage is characterized by the following traction-separation parameters:

$$\begin{aligned}
\delta_m &= \sqrt{(\delta_{22})^2 + (\delta_{12})^2} \\
\sigma_m &= \sqrt{(\sigma_{22})^2 + (\sigma_{12})^2} \\
G_{Cm} &= G_{C22} + (G_{C12} - G_{C22})\left(\frac{G_{12}}{G_{22} + G_{12}}\right)^\eta
\end{aligned} \tag{10}$$

where G_{Cij} are the critical fracture energies ($i, j = 1$ or 2).

The *post-damage* state is defined by a prescribed critical damage $D_{max} = \left(1 - \sigma_{ij}/\sigma_{ij}^{crit}\right)$, that is unique for all the five damage modes described in the model. These are fiber rupture under tension, fiber kinking under compression, matrix cracking and fiber–matrix debonding under tension, matrix cracking under transverse compression, and matrix shear cracking.

In this model, the *element elimination* is based on the equivalent shear strain limit $\varepsilon_{elim} = \varepsilon_{ij} - (1/3)\varepsilon_{kk}\delta_{ij}$ ($i, j, k = 1$ or 2).

2.4. Delaminations

Capturing all the failure modes of a crashing structure requires the use of a multi-shell model to obtain not only the failure of the composite plies but also the delaminations of the interlaminar interfaces. In ESI-VPS, these interactions can be modeled as 1D beams (called TIED elements, Fig. 3) connecting nodes and elements belonging to two adjacent surfaces. Main interlaminar damage properties derive from Mode I and Mode II experimental tests and follow the classic traction-separation law [22] where the initial (δ_I^i and δ_{II}^i) and final (δ_I^f and δ_{II}^f) separation values are calculated as follows:

$$\delta_I^i = \frac{\sigma_I^{max}}{E_0} \quad \text{and} \quad \delta_I^f = \frac{2G_{IC}}{\sigma_I^{max}} \quad for \quad \text{Mode I}$$

$$\delta_{II}^i = \frac{\sigma_{II}^{max}}{G_{12}} \quad \text{and} \quad \delta_{II}^f = \frac{2G_{IIC}}{\sigma_{II}^{max}} \quad for \quad \text{Mode II}$$
(11)

where σ_I^{max} is the interlaminar tensile strength, σ_{II}^{max} is the interlaminar shear strength, E_0 and G_{12} are the Young's modulus and the shear modulus, G_{IC} and G_{IIC} are the fracture toughness in Mode I and Mode II, respectively.

The mixed-mode interaction can then be implemented either using the well-known Benzeggagh-Kenane Eq. (12) or the power law model (13) [21,23], expressed by means of the following equations:

$$G_{IC} + (G_{IIC} - G_{IC})\left(\frac{G_i^{II}}{G_i^{II} + G_i^I}\right)^{\eta} = G_C$$
(12)

$$\left(\frac{G_i^I}{G_{IC}}\right)^{\eta} + \left(\frac{G_i^{II}}{G_{IIC}}\right)^{\eta} = 1$$
(13)

3. Damage calibration and modeling strategies

Every damage model needs proper calibrations to obtain reliable results. However, usually the FEM software manuals only provide a brief description of the theoretical working of the damage models, and accurate calibration is often left to the user for the specific cases of interest.

Moreover, mesh layout, boundary conditions, and contact algorithms highly influence the model outcomes and should be optimized for the specific model implementation to obtain results as close as possible to reality.

In the following paragraphs, the calibration approaches for the Ladevèze and Waas-Pineda damage models for unidirectional plies are described. In addition, the authors' modeling strategies to obtain reliable crushing simulations are proposed.

3.1. Damage models calibration procedures

As explained in §2.2, the *LV model* needs material parameters, deriving from experimental characterization, and specific numerical parameters, calibrated iteratively from numerical simulations.

To achieve reliable results, quasi static tests in tension (ASTM D3039 [24]), compression (ASTM D3410 [25]) and in-plane shear (ASTM D3518 [26]) as well as cyclic in-plane tests are necessary.

From quasi-static tension and compression tests, the undamaged Young's moduli E_{kk}^{0j}, the stress values $\sigma_{kk,i}^j$ at first nonlinearity, the ultimate failure stresses $\sigma_{kk,u}^j$ (*k* indicates the direction of the property, *j* is equal to *t* or *c* for tension or compression tests) are obtained. In-plane shear tests allow the measure of the material shear properties (shear modulus G_{12}, ultimate shear stress σ_{12}, shear strain ε_{12}).

Cyclic in-plane shear tests are then essential to calculate the conjugate forces Y_i. These tests are conducted in accordance with the ASTM D3518 and involve carrying out a series of loading and unloading cycles with increasing relative maximum load. A minimum of five cycles are required for calculation accuracy, while a maximum of ten cycles limits the low cycle fatigue effects. In each cycle, the
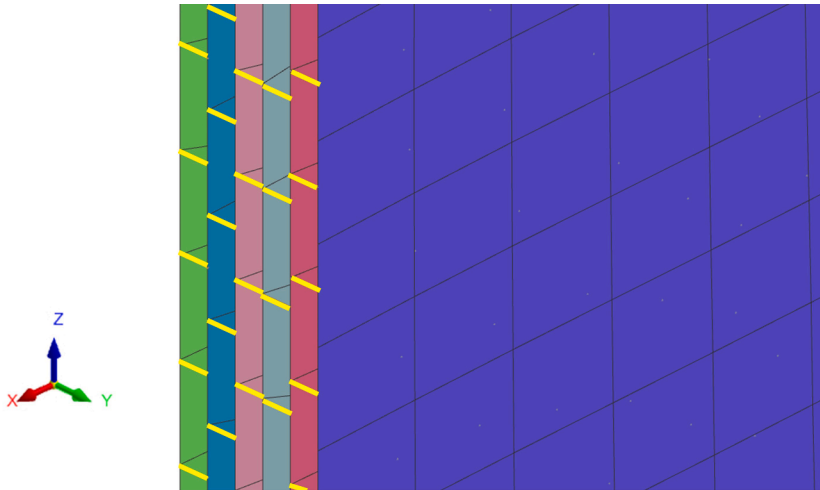

Fig. 3. 1D beam elements (yellow). (For interpretation of the references to colour in this figure legend, the reader is referred to the web version of this article.)

damaged modulus is calculated; damage parameter and conjugate force derive from (4) that can be written as a function of the elastic strain at i-th cycle, $Y_i(\varepsilon^e_{12,i})$. Plotting the damage parameter d_i as a function of the conjugate force Y_i for each i-th cycle, it is possible to interpolate the curve $Y_i = f(d_i)$ and calculate the needed damage parameters. Moreover, the matrix plasticity parameters are obtained from the interpolation of the $R_i(p)$ curve.

The damage parameters should be then validated by simulating the experimental tests and comparing the outputs with the test results.

Lastly, the best-fit value for the limit strains ε_{lim} has to be determined iteratively by comparing experimental and numerical results of Compact Tension (CT) and Compact Compression (CC) tests.

Similarly to the LV damage model, the *WP damage model* employs many material parameters, obtained through experimental mechanical characterization tests, and few numerical parameters needed to stabilize the simulation.

Quasi-static tests are necessary to determine ultimate stresses under tension, compression, and shear load ($\Sigma_{kk,t}$, $\Sigma_{kk,c}$ and T_{12} respectively). Stiffness moduli are calculated as well: longitudinal and transversal Young's moduli in tension and compression ($E_{kk,t}$ and $E_{kk,c}$) in addition to the shear modulus (Γ_{12}) from in-plane shear tests.

The ultimate stress values are considered as stress thresholds for damage initiation, and it is possible to define different damage initiation thresholds for tension, compression, and shear loading conditions.

CC and CT tests are then performed to evaluate the intralaminar fiber fracture energies. These values are applied in the model and the whole set of experimental tests is simulated to verify the numerical implementation. As suggested by Pinho et al. in [27], however, transversal and shear intralaminar fracture energies can also be obtained from interlaminar Mode I and Mode II tests. In particular, $G_{22,t}$ can be set equal to G_{IC}, while $G_{22,c}$ and G_{12} can be set equal to G_{IIC}.

The last step of the calibration procedure for the WP damage model consists of the determination of the maximum damage (D_{max}) and the element elimination parameter (ε_{elim}) to fulfill the numerical stability of the crashing simulation. This is achieved through a tuning process. It is important to consider that setting high ε_{elim} values may result in an unsuccessful element elimination, leading to unstable simulations. Conversely, low ε_{elim} values may cause an early and uncontrolled element elimination. On the other hand, it is recommended to set a high D_{max} value to ensure greater stability and obtain more accurate outcomes. It is recommended to use ε_{elim} between 0.15 and 0.3 and D_{max} between 0.6 and 0.9: it has been observed that values within these ranges work properly in most situations.

The interlaminar properties for Mode I and Mode II failure modes (G_{IC} and G_{IIC}, respectively) are measured by means of Double Cantilever Beam (DCB, ASTM D5528 [28]) and End Notched Flexure (ENF, ASTM D7905 [29]) tests. For Mode I toughness, it is suggested to consider only the initiation threshold, as the propagation values may be influenced by fiber bridging at the interfaces.

Table 1 provides a summary of the required experimental tests, along with the corresponding parameters for the damage models.

3.2. Mesh and boundary conditions

In the majority of Finite Element software, the default mesh type is the uniformly structured mesh, usually aligned with the principal geometry direction. However, for crush tests, this results in unstable loads and unreliable output: in fact, when an aligned row of elements is loaded, all the elements reach the damage thresholds together, as well as the elimination value, and are removed simultaneously. Therefore, the contact between the crushing wall and the component is lost and the compression is released until contact is reestablished. This discontinuous load generates a high-intensity pressure wave traveling across the part. Since no dissipation is introduced, these pressure waves quickly accumulate and generate spurious load peaks, ultimately leading to undesired failure.

To overcome this issue, an unstructured or skewed mesh is suggested (Fig. 4). In this way, the elements are eliminated gradually as the crushing wall advances, effectively assuring the continuity in the contact between the wall and the specimens and reducing the load oscillations.

Mesh convergence for interlaminar damage and measures to compensate for mesh sensitivity of ply damage were investigated in previous works from the authors [30,5] respectively. The need for a mesh insensitive formulation when using non-local damage models was also investigated by Reiner et al. [31,32]. Notably, when unstructured meshes are generated only a target average element side length is achieved, while small local variations in element size is present and to be expected. Nevertheless, their scatter is small, and the global behavior is not influenced by these small variations.

Each experimental test simulation (whose results are described in §4) should include boundary conditions that replicate the test

Table 1
Input parameters derived from experimental tests.

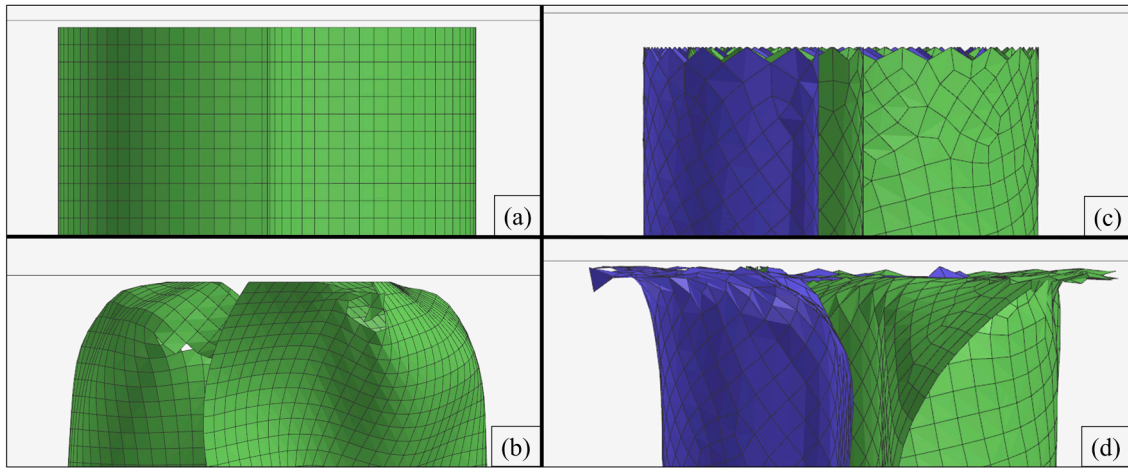| Test	Base material	LV Model	WP Model
Tensile	$E^{0t}_{11}, E^{0t}_{22}, \nu_{12}$	$Y_{110}, Y_{11c}, Y_{11f}$	$\Sigma_{11t}, \Sigma_{22,t}$
Compressive	E^{0c}_{11}, E^{0c}_{22}	$Y^c_{110}, Y^c_{11c}, Y^c_{11f}$	$\Sigma_{11,c}, \Sigma_{22,c}$
In-plane	G^0_{12}, R_0, β, m	$Y_{120}, Y_{12c}, Y_{12f}, \varepsilon_{12lim}$	T_{12}, G_{12}
CC		$\varepsilon_{11,clim}, \varepsilon_{22,clim}$	G_{11c}
CT		$\varepsilon_{11,tlim}, \varepsilon_{22,tlim}$	G_{11t}
DCB			G_{22t}
ENF			G_{22c}, G_{12}

Fig. 4. Examples of structured (a, b) and skewed (c, d) meshes: one shell for structured and two shells for skewed meshes are shown to highlight undesired (b) and proper (d) crash failures.

conditions.

In the case of tension, in-plane shear and compression, the testing fixture is simulated by fixing the proper degree of freedom of the nodes at the ends of the coupon. The testing velocity is applied to one end of the specimen while the other is fixed: this adequately represents the real testing conditions (Fig. 5). For these simulations, the model consists of a single shell that reproduces the entire stacking sequence, with a mesh size of 1 mm. The tensile and compression simulations take less than 10 min to complete, while the in-plane shear model takes approximately 20 min.

For CC and CT tests, the coupon is loaded by a displacement applied on the loading holes (Fig. 6). At the same time, the other nodes cannot move out of the specimen plane, simulating the external guides used during the experimental test to avoid out-of-plane bending. CC and CT models are composed of a single shell which models the entire stacking sequence. The mesh size around the crack tip is set to 0.25 mm, and the run time is approximately 2.5 h each.

In DCB tests, the pre-cracked area, which is experimentally obtained by using a thin release film in the middle of the stacking sequence, is modeled as an area between the two shells (each representing half of the specimen, Fig. 7) without interlaminar beam elements (TIED); the load is applied to both halves of the specimen. Average run time is approximately 30 min using a 1 mm mesh size.

Finally, the crash tests are performed on corrugated self-supporting specimens. These specimens, as described by Feraboli in [33], have the advantage of not requiring additional anti-buckling fixtures. To ensure a stable crushing behaviour, during experimental tests, a 45° central chamfer trigger was crafted on the loading edge of the specimens. Nominal section dimensions are reported in Fig. 8, while specimen height is 80 mm.

For crush simulations, test geometries are modelled using the stacked shell approach [34], which has been successfully adopted in multiple scenarios where delamination damage and extensive ply sliding is expected [35,36]. This allows to retain a higher physical
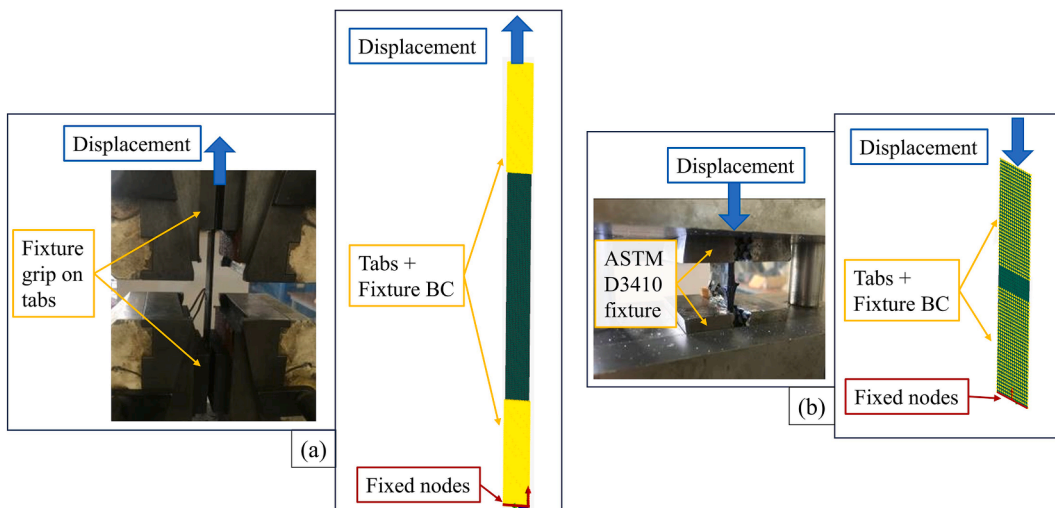

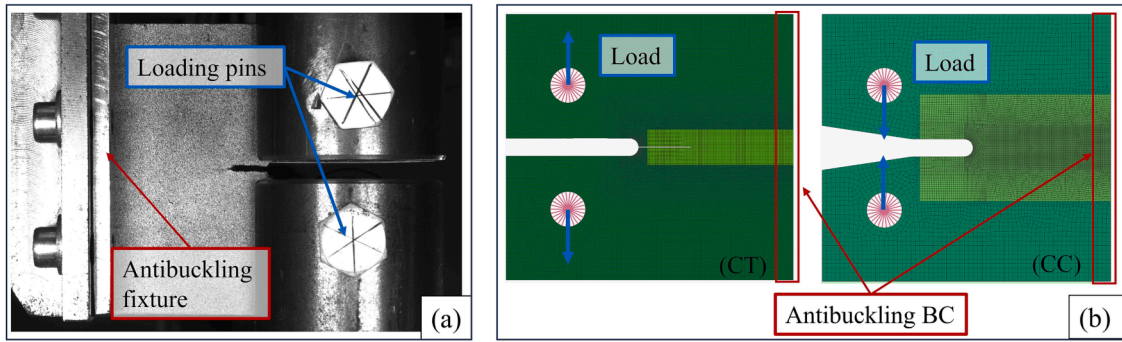**Fig. 5.** Experimental and numerical conditions: (a) tension and in-plane shear, (b) compression.

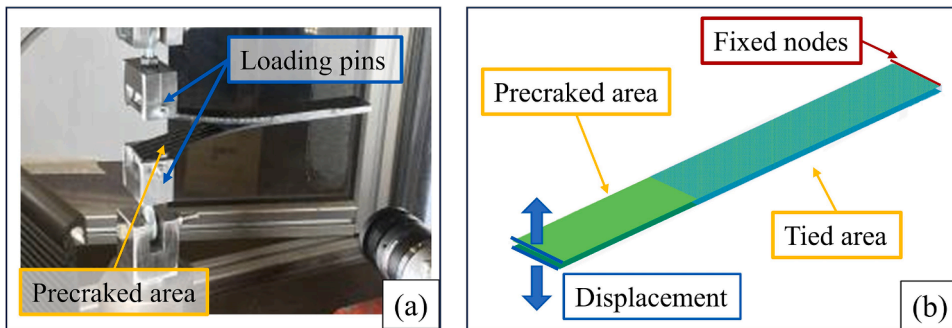**Fig. 6.** Experimental (a) and numerical (b) conditions for CT and CC tests.

Fig. 7. Experimental (a) and numerical (b) conditions for DCB tests.

fidelity compared to single shell models and homogenized solid elements models. The inclusion of delamination effects opens the possibility to visually compare the morphology of crushing and identify weaknesses in the geometries that would not be possible with more simplified methods. At the same time, the computational cost is kept relatively low: the geometries described in this work are represented with less than 2.0×10^5 degrees of freedom, explicit time increments higher than 1.0×10^{-4} ms, and every run takes approximately 30 min to complete.

The specimen is modeled with six shells, each representing a bundle of two plies with the same fiber orientation, and five inter-laminar beam elements (TIED) layers, representing the interfaces between plies. The crushing dynamic is represented by imposing a constant velocity to a rigid plate moving towards the free end of the composite part. The constrained end of the specimen is simulated by fixing all the translational degrees of freedom of the last row of nodes. A graphical representation is shown in Fig. 9.

3.3. Contact properties

In order to obtain a reliable crushing simulation, two different contact properties are necessary. First of all, a symmetric master–slave node-to-segment/edge contact algorithm between the specimen and the crushing wall is required. In addition, a self-impacting node-to-segment/edge contact between adjacent plies is needed whenever the laminate is represented by multiple stacked shells. Both contacts use a penalty algorithm. ESI-VPS automatically handles the coexistence of contact and TIED elements by activating the self-contact locally. In particular, the contact between adjacent shells is initially disabled for every node with active connectivity to a TIED link. Contact is then activated locally only when the TIED element linked to each node is deactivated or eliminated due to damage.

Friction coefficients equal to 0.2 for the shell-to-wall contact and 0.4 for the self-contact were used: these values determine a crush
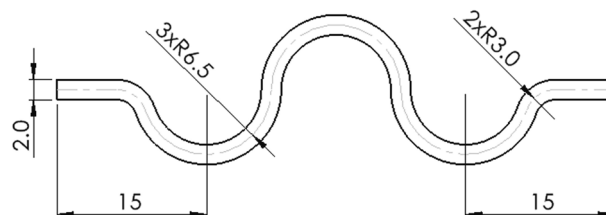

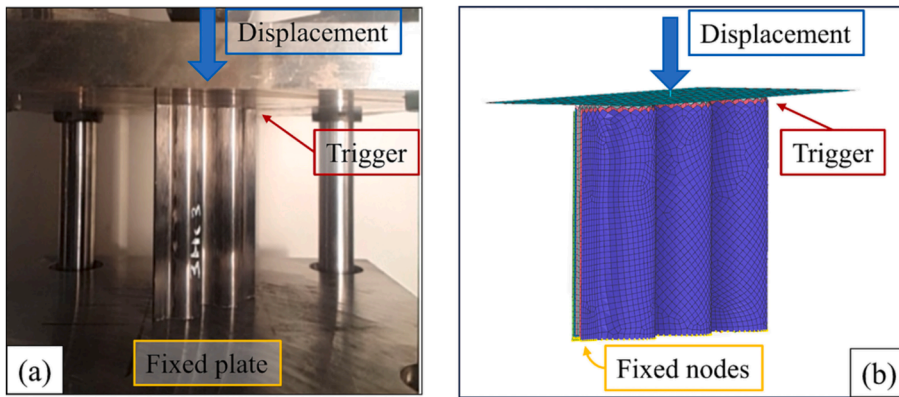**Fig. 8.** Section drawing of the self-supported specimen (dimensions in mm).

Fig. 9. Crash test example: (a) experimental, (b) numerical boundary conditions.

morphology most similar to experimental evidence, as demonstrated in the literature [8,14,37,38].

4. Numerical-experimental comparison

Experimental tests are performed both for parameters calculation and model calibration. The test specimens used in this work were manufactured with T700-DT120-UD prepreg by means of hand-layup and autoclave cure. Specimen geometry and thickness differ for each mechanical characterization test according to the corresponding regulations. Five specimens per each characterization were tested. The main results are summarized in the following sections, specifically focusing on the parameters needed to populate the material cards (Tables 2 and 3).

4.1. Static tests

By means of static tension tests (ASTM D3039 [24]) on $[0]_8$ and $[90]_8$ specimens and compression tests (ASTM D3410 [25]) on $[0]_{20}$ and $[90]_{20}$ specimens, the Young's moduli along the longitudinal and the transversal direction, the stresses and strains at failure, and the Poisson ratios were measured.

The micro-buckling parameter (γ), describing the non-linear behavior in compression, was calculated as previously described. The comparison between numerical simulations and experimental results is presented in Fig. 10: a good agreement between the experimental and numerical curves can be spotted in both tension (a) and compression (b) loading cases.

4.2. Cyclic in-plane tests

The matrix damage and plasticization were characterized by means of cyclic in-plane shear tests (ASTM D3518 [26]) performed on $[45/-45]_{2s}$ specimens. The value of the shear modulus was obtained per each i-th cycle (G_{12}^i) and the damage calculated as $d_i = 1 - G_{12}^i/G_{12}^0$, where G_{12}^0 is the undamaged shear modulus. From these values, knowing that the parameter Y can be computed as:

Table 2
Ladevèze ply material card - main parameters.

Experimental tests	Property	Parameter	Value
Tensile	Elastic modulus - longitudinal	E_{11}^{0t}	135.5 GPa
	Elastic modulus - transversal	E_{22}^{0t}	14.5 GPa
	Poisson modulus	ν_{12}	0.295
Shear tension	Shear modulus	G_{12}^0	4.95 GPa
	Plasticity threshold stress	R_0	30 MPa
	Plasticity multiplicative factor	β	1.6804 GPa
	Plasticity exponential factor	m	0.5465
Cyclic shear tension	Initial shear damage	Y_0	0.0094 GPa$^{0.5}$
	Critical shear damage	Y_c	0.024 GPa$^{0.5}$
Compressive	Elastic modulus	E_{11}^{0c}	111.2 GPa

Table 3
Waas-Pineda damage model - main parameters.

Experimental tests	Property	Parameter	Value
Tensile	Tensile axial limit	$\Sigma_{11,t}$	1.76 GPa
	Tensile transverse limit	$\Sigma_{22,t}$	56 MPa
Compressive	Compressive axial limit	$\Sigma_{11,c}$	820 MPa
	Compressive transverse limit	$\Sigma_{22,c}$	185 MPa
Shear tension	Shear limit	T_{12}	43.5 MPa
Fracture toughness	Axial tensile fracture energy	$G_{11,t}$	0.105 J/mm^2
	Axial compressive fracture energy	$G_{11,c}$	0.082 J/mm^2
	Transverse tensile fracture energy	$G_{22,t}$	0.00047 J/mm^2
	Transverse compressive fracture energy	$G_{22,c}$	0.00179 J/mm^2
	Shear fracture energy	G_{12}	0.00179 J/mm^2
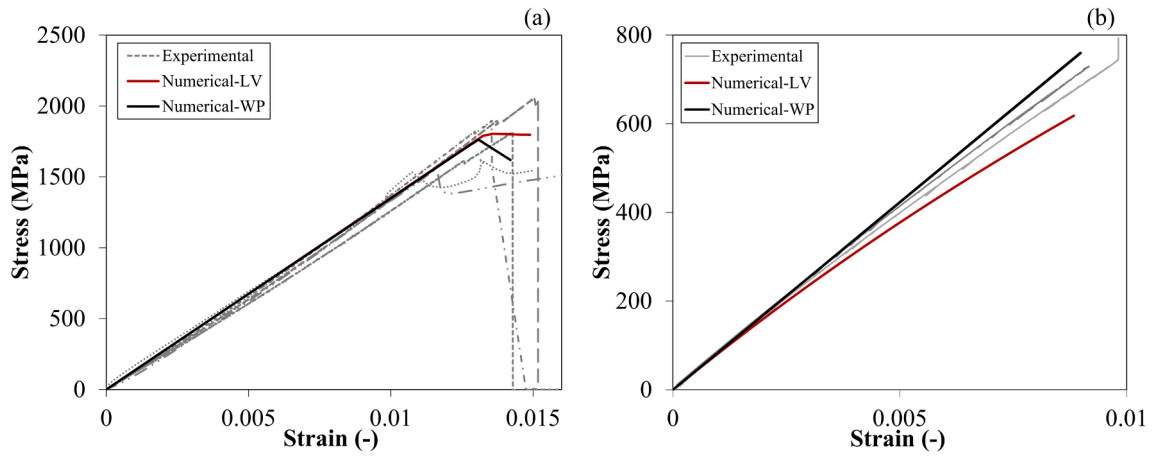
Fig. 10. Tension (a) and compression (b) tests: numerical-experimental comparison. Five experimental curves are showed in tension, two in compression.

$$Y_i = \sqrt{\frac{1}{2}G_{12}^0\left(2\varepsilon_{12,i}^e\right)^2} \tag{14}$$

it is possible to rearrange the equation as $Y_i = Y_0 + Y_c d_i$, to obtain the initial damage threshold Y_0 and the critical damage Y_C. For the matrix plasticity, the sum of the yield strength R_0 and the hardening function R_i is:

$$R_0 + R_i = \frac{\sigma_{12}^i}{1-d_i} \tag{15}$$

while the effective plastic strain p_i can be expressed as:

$$p_i = \int_0^{\varepsilon_{12}^p} (1-d_i)d\varepsilon_{12,i}^p \tag{16}$$

where $\varepsilon_{12,i}^e$ is the elastic strain at i-th cycle ($\varepsilon^e = \varepsilon - \varepsilon^p$, with ε the total strain and ε^p the residual plastic strain at zero stress). Rearranging (15) as a power function of p, it is possible to interpolate the function $R(p) = \beta p^m$ to calculate the parameters β and m.

The comparison between experimental, analytical, and numerical results for the cyclic in-plane tests is presented in Fig. 11. Notably, whereas here LV is able to replicate the laminate behavior at every point, WP differs significantly. This is a consequence of the model imposing a softening cohesive-like behavior to every damage mode and is to be expected for this type of tests. The equivalence with the experimental results can only be interpreted in terms of strain-energy to failure.

4.3. Interlaminar tests

Mode I and Mode II fracture toughness values were obtained through Double Cantilever Beam (DCB) and End-Notched Flexure
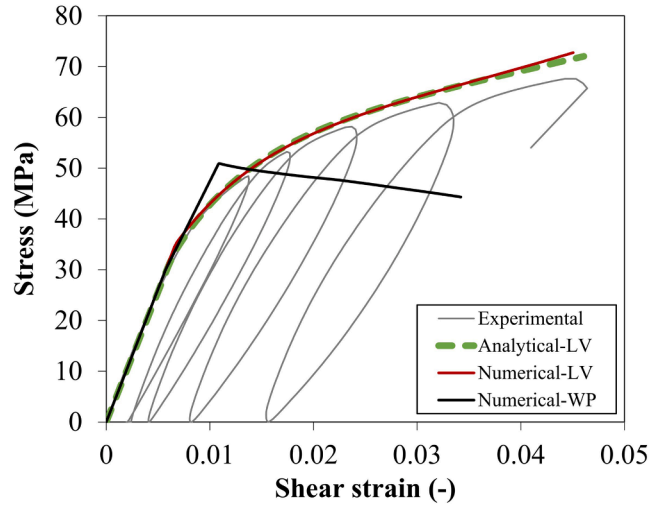
Fig. 11. In-plane shear tests: experimental, analytical, and numerical comparison.

(ENF) tests, respectively. Test coupons are obtained from a $[0]_{24}$ laminate. The damaging interlaminar interaction is simulated with cohesive traction-separation formulation by means of TIED beam elements in ESI-VPS [21]. A description of the inner working of TIED elements is also found in [13].

The Mode I and Mode II toughness values obtained were 470 J/m^2 and 1790 J/m^2, respectively. The comparison between numerical and experimental DCB results is shown in Fig. 12.

4.4. Compact tension and compact compression

The intralaminar fracture energy can be measured through many test methods, among which the most valuable ones are the CT and the CC tests [39,40]. As already seen in §2.2.1 and §2.3.1, these tests are essential in both LV and WP models. In the first case, simulations are used to iteratively tune the value of the element elimination parameter ε_{lim}, assuring numerical stability. In the WP model, instead, they allow tuning the fiber fracture energy values. The tuning process involves iteratively adjusting the elimination parameter and fiber fracture energy values until an improved representation of experimental tests is obtained. This can be done either manually or through a look-up table algorithm. The authors in this work opted for a manual tuning process.

Fig. 13 shows the comparison between experimental CT and CC tests and the numerical simulations (obtained after parameters optimization) results. Simultaneously, Fig. 14 shows the comparison between the experimental and numerical crack growth.
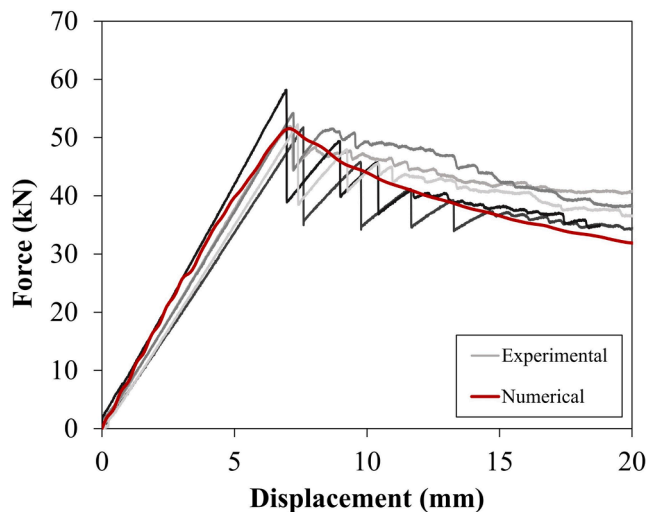

Fig. 12. DCB tests: experimental and numerical comparison. Five experimental tests are shown.
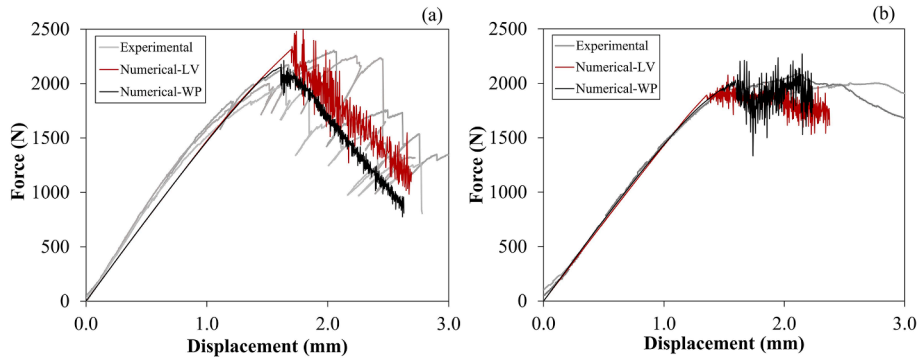
Fig. 13. CT (a) and CC (b) tests: experimental–numerical comparison. Three experimental curves are shown.

4.5. Crashworthiness

In order to verify the effectiveness of the calibration procedures, compressive crush tests were performed on $[0_2/90_2/0_2]_s$ corrugated self-supporting specimens. From the compressive crush tests (Fig. 15), Load-Displacement curves were obtained, as well as the Specific Energy Absorption (SEA) values. This parameter measures the energy dissipated due to the damaging, normalized by the weight of the material participating in the crushing. In the literature, different methods are used to calculate the SEA [6]; in this work, due to the intrinsic difference between numerical and physical triggers, the value used for comparison is the Steady-State SEA (SEA_{ss}). This excludes the transient region that includes the initial compression and the force peak observed in the first millimeters of displacement, defined by x_0 in the formula below:

$$SEA_{ss}(x_c) = \frac{\int_{x_0}^{x_c} f dx}{m(x_c - x_0)/h}$$

(17)

where f is the sustained crush force, m and h the coupon weight and height, and x_c the total displacement value used for computation.

As shown in Fig. 16-a, the numerical simulations capture the main crushing failure modes: delaminations and splaying lamina bundles. In addition, Fig. 16-b shows a good agreement between the Load-Displacement curves with the two numerical models and the experimental tests.

For the steady-state portion of the Load-Displacement curves, the crush behavior in the range between 3 and 8 mm is correctly captured by both numerical models. Instead, the damage models tend to underestimate the experimental load resistance at higher displacements. This phenomenon is attributed to the necessity to include numerical element erosion at complete failure. In fact, post-mortem observation of crushed specimens indicates that the fragmented debris, confined in the central wedge between splayed plies, play a significant role in the overall crushing behavior and load bearing. At the current stage, it is not possible to include this phenomenon in a numerical simulation at the constitutive model level. Instead, this behavior is usually obtained with ad-hoc techniques like adding specific dissipative elements or introducing extraneous rigid body elements in the wedge region with additional friction behavior. However, a downside of these techniques is that they need ex-post calibration, increasing the deviation from a realistic representation. Therefore, they are ultimately not suited for a predictive tool and are not investigated further.

The behavior of the component within the range of 0 to 3 mm cannot be considered representative of its energy absorption capacity.
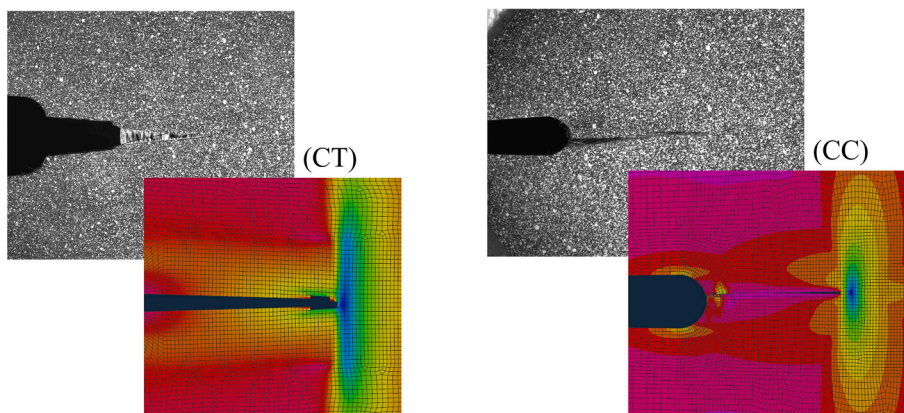

Fig. 14. Compact tension and compact compression tests crack growth: experimental–numerical comparison.
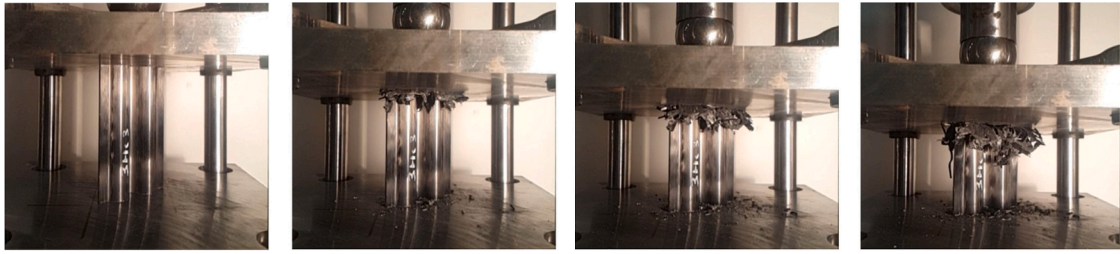
Fig. 15. Sample screenshots of one compressive crush test.
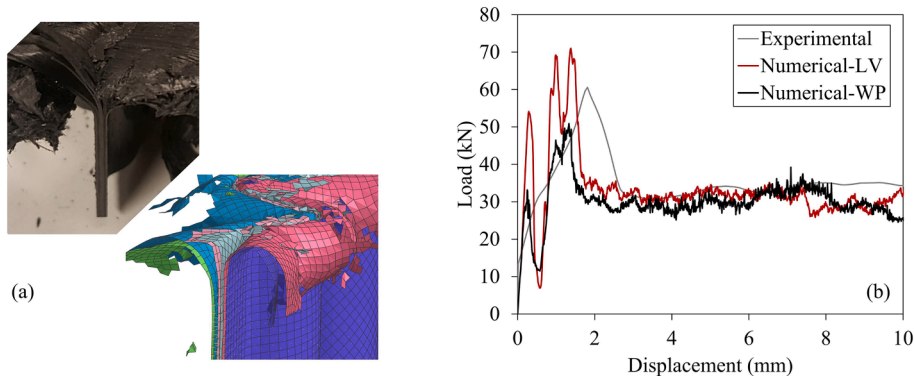

Fig. 16. Comparison of crash test experimental–numerical results: left side, failure mode; right side, load-displacement curves.

This is due to the variability in the geometry of the trigger during the manufacturing stage, as well as the differences in its numerical modeling. Therefore, it is not possible to draw any meaningful conclusions based on this initial behavior. Additionally, the primary focus of the proposed method is to illustrate the Steady-State crushing process while disregarding any transient and unstable behavior.

In conclusion, in the limited displacement range indicated above, the average Steady-State SEA of the tested samples is equal to 102.7 J/g (the standard deviation is 7.5 J/g, corresponding to a 7.3 % variation), while simulated values are 95.9 J/g (Waas-Pineda model) and 98.5 J/g (Ladevèze model). This slight difference (6.6 % and 4.1 % for WP and LV, respectively) supports the good agreement of the results and proves the reliability of the model and calibration procedures.

5. Conclusions

This paper provides a concise theoretical overview and detailed specific calibration procedures for Ladevèze and Waas-Pineda damage models for unidirectional laminae. These particular implementations are based on individual lamina (or sub-laminate) properties, including interlaminar fracture, therefore retaining more physical detail of the crush phenomenology than a purely energy-based simulation. The proposed guidelines, related to the damage models' calibration and simulation strategies, ensure a reliable set-up for crashworthiness simulations by means of ESI-VPS Crash PAM. The related experimental mechanical material characterization campaign is briefly described, focusing on straightforward methods for deriving the parameters required to populate the material cards as presented in the software. Using this data, numerical simulations tailored for calibration and validation are performed. A good agreement is found between tests and simulations, supporting the reliability of the proposed calibration methods. These procedures are, therefore, ready for further implementation into more complex geometries and load cases.

CRediT authorship contribution statement

M.P. Falaschetti: Conceptualization, Methodology, Formal analysis, Investigation, Data curation, Writing – original draft, Writing – review & editing. **F. Rondina:** Methodology, Validation, Investigation, Writing – review & editing. **N. Zavatta:** Formal analysis, Resources, Writing – review & editing. **E. Troiani:** Methodology, Supervision, Project administration, Funding acquisition. **L. Donati:** Methodology, Supervision, Writing – review & editing, Funding acquisition.

Declaration of competing interest

The authors declare that they have no known competing financial interests or personal relationships that could have appeared to influence the work reported in this paper.

Data availability

The data that support the findings of this study are available on request from the corresponding author.

Acknowledgments

References

[1] P.H. Thornton, Energy absorption in composite structures, J. Compos. Mater. 13 (1979) 247–262, https://doi.org/10.1177/002199837901300308.
[2] D. Cocchi, L. Raimondi, T.M. Brugo, A. Zucchelli, A systematic material-oriented design approach for lightweight components and the CFRP motor wheel case study, Int. J. Adv. Manuf. Technol. 109 (2020) 2133–2153, https://doi.org/10.1007/S00170-020-05756-2/FIGURES/20.
[3] E. Troiani M.P. Falaschetti S. Taddia A. Ceruti CFRP crash absorbers in small UAV: design and optimization. Sae Tech. Pap., vol. 2015- September, SAE Int. 2015. https://doi.org/10.4271/2015-01-2461.
[4] S. Ramakrishna, Microstructural design of composite materials for crashworthy structural applications, Mater. Des. 18 (1997) 167–173, https://doi.org/10.1016/S0261-3069(97)00098-8.
[5] F. Rondina, M.P. Falaschetti, N. Zavatta, L. Donati, Numerical simulation of the compression crushing energy of carbon fiber-epoxy woven composite structures, Compos. Struct. 303 (2023) 116300, https://doi.org/10.1016/j.compstruct.2022.116300.
[6] M.P. Falaschetti, F. Rondina, E. Maccaferri, L. Mazzocchetti, L. Donati, A. Zucchelli, et al., Improving the crashworthiness of CFRP structures by rubbery nanofibrous interlayers, Compos. Struct. 311 (2023) 116845, https://doi.org/10.1016/J.COMPSTRUCT.2023.116845.
[7] E. Troiani, L. Donati, G. Molinari, R. Di Sante, Influence of plying strategies and trigger type on crashworthiness properties of carbon fiber laminates cured through autoclave processing, Stroj Vestnik/J. Mech. Eng. 60 (2014) 375–381, https://doi.org/10.5545/SV-JME.2013.1506.
[8] A.G. Mamalis, D.E. Manolakos, M.B. Ioannidis, D.P. Papapostolou, On the experimental investigation of crash energy absorption in laminate splaying collapse mode of FRP tubular components, Compos. Struct. 70 (2005) 413–429, https://doi.org/10.1016/J.COMPSTRUCT.2004.09.002.
[9] M.P. Falaschetti, M. Scafé, N. Zavatta, E. Troiani, Hygrothermal ageing influence on BVI-damaged carbon/epoxy coupons under compression load, Polymers 13 (2021) 2038, https://doi.org/10.3390/POLYM13132038.
[10] N. Zavatta, F. Rondina, M.P. Falaschetti, L. Donati, Effect of thermal ageing on the mechanical strength of carbon fibre reinforced epoxy composites, Polymers 13 (2021) 2006, https://doi.org/10.3390/POLYM13122006.
[11] F.K. Chang, K.Y. Chang, A Progressive Damage Model for Laminated Composites Containing Stress Concentrations Http://DxDoiOrg/101177/002199838702100904 21 (2016) 834–855. doi:10.1177/002199838702100904.
[12] P. Feraboli, B. Wade, F. Deleo, M. Rassaian, M. Higgins, A. Byar, LS-DYNA MAT54 modeling of the axial crushing of a composite tape sinusoidal specimen, Compos. A Appl. Sci. Manuf. 42 (2011) 1809–1825, https://doi.org/10.1016/J.COMPOSITESA.2011.08.004.
[13] A.F. Johnson, A.K. Pickett, P. Rozycki, Computational methods for predicting impact damage in composite structures, Compos. Sci. Technol. 61 (2001) 2183–2192, https://doi.org/10.1016/S0266-3538(01)00111-7.
[14] V.S. Sokolinsky, K.C. Indermuehle, J.A. Hurtado, Numerical simulation of the crushing process of a corrugated composite plate, Compos. A Appl. Sci. Manuf. 42 (2011) 1119–1126, https://doi.org/10.1016/J.COMPOSITESA.2011.04.017.
[15] N. Germain, J. Besson, F. Feyel, Composite layered materials: anisotropic nonlocal damage models, Comput. Methods Appl. Mech. Eng. 196 (2007) 4272–4282, https://doi.org/10.1016/J.CMA.2007.04.009.
[16] N. Zobeiry, A. Forghani, C. McGregor, S. McClennan, R. Vaziri, A. Poursartip, Effective calibration and validation of a nonlocal continuum damage model for laminated composites, Compos. Struct. 173 (2017) 188–195, https://doi.org/10.1016/J.COMPSTRUCT.2017.04.019.
[17] P. Ladevèze, O. Allix, L. Gornet, D. Lévêque, L. Perret, A computational damage mechanics approach for laminates: identification and comparison with experimental results, Stud. Appl. Mech. 46 (1998) 481–500, https://doi.org/10.1016/S0922-5382(98)80059-7.
[18] E.A. Pineda, Novel Multiscale Physics-Based Progressive Damage and Failure Modeling Tool for Advanced Composite Structures [Ph.D. Thesis], University of Michigan, 2012.
[19] E.J. Pineda, A.M. Waas, Numerical implementation of a multiple-ISV thermodynamically-based work potential theory for modeling progressive damage and failure in fiber-reinforced laminates, Int. J. Fract. 182 (2013) 93–122, https://doi.org/10.1007/S10704-013-9860-1/FIGURES/19.
[20] A.G. Mamalis, D.E. Manolakos, M.B. Ioannidis, D.P. Papapostolou, Crashworthy characteristics of axially statically compressed thin-walled square CFRP composite tubes: experimental, Compos. Struct. 63 (2004) 347–360, https://doi.org/10.1016/S0263-8223(03)00183-1.
[21] ESI-Software, Virtual Performance Solution Solver Reference Manual. 2022ed ed. n.d.
[22] P.P. Camanho, C.G. Davila, Mixed-mode decohesion finite elements for the simulation of delamination in composite materials, 2002.
[23] M.L. Benzeggagh, M. Kenane, Measurement of mixed-mode delamination fracture toughness of unidirectional glass/epoxy composites with mixed-mode bending apparatus, Compos. Sci. Technol. 56 (1996) 439–449, https://doi.org/10.1016/0266-3538(96)00005-X.
[24] ASTM standard. ASTM D3039/D3039M-08 Standard Test Method for Tensile Properties of Polymer Matrix Composite Materials. ASTM Int, 2008.
[25] ASTM standard. ASTM D3410/D3410M: Standard Test Method for Compressive Properties of Polymer Matrix Composite Materials with Unsupported Gage Section by Shear Loading. ASTM Int 16 (1997) 29.
[26] ASTM standard. ASTM D3518: Standard Test Method for In-Plane Shear Response of Polymer Matrix Composite Materials by Tensile Test. ASTM Stand 94 (2007) 1–7.
[27] S.T. Pinho, P. Robinson, L. Iannucci, Fracture Toughness of the Tensile and Compressive Fibre Failure Modes in Laminated Composites, 2006. doi:10.1016/j.compscitech.2005.12.023.
[28] ASTM standard, ASTM D5528-13: standard test method for mode I interlaminar fracture toughness of unidirectional fiber-reinforced polymer matrix composites, Am. Stand. Test Methods 03 (2014) 1–12.
[29] ASTM standard. ASTM D7905: Standard test method for determination of the mode II interlaminar fracture toughness of unidirectional fiber-reinforced polymer matrix composites, ASTM 2014, pp. 1–18.
[30] F. Rondina, L. Donati, Comparison and validation of computational methods for the prediction of the compressive crush energy absorption of CFRP structures, Compos. Struct. 254 (2020) 112848, https://doi.org/10.1016/j.compstruct.2020.112848.
[31] J. Reiner, T. Feser, M. Waimer, A. Poursartip, H. Voggenreiter, R. Vaziri, Axial crush simulation of composites using continuum damage mechanics: FE software and material model independent considerations, Compos. B Eng. 225 (2021) 109284, https://doi.org/10.1016/J.COMPOSITESB.2021.109284.
[32] J. Reiner, R. Vaziri, N. Zobeiry, Machine learning assisted characterisation and simulation of compressive damage in composite laminates, Compos. Struct. 273 (2021) 114290, https://doi.org/10.1016/J.COMPSTRUCT.2021.114290.
[33] P. Feraboli, Development of a corrugated test specimen for composite materials energy absorption, J. Compos. Mater. 42 (2008) 229–256, https://doi.org/10.1177/0021998307086202.

[34] S. Heimbs, S. Heller, P. Middendorf, F. Hähnel, J. Weiße, Low velocity impact on CFRP plates with compressive preload: test and modelling, Int. J. Impact Eng. 36 (2009) 1182–1193, https://doi.org/10.1016/J.IJIMPENG.2009.04.006.

[35] F. Vannucchi de Camargo, A. Pavlovic, E.C. Schenal, C. Fragassa, Explicit stacked-shell modelling of aged basalt fiber reinforced composites to low-velocity impact, Compos. Struct. 256 (2021) 113017, https://doi.org/10.1016/J.COMPSTRUCT.2020.113017.

[36] G.M.K. Pearce, A.F. Johnson, A.K. Hellier, R.S. Thomson, A Stacked-Shell Finite Element Approach for Modelling a Dynamically Loaded Composite Bolted Joint Under in-Plane Bearing Loads n.d. https://doi.org/10.1007/s10443-013-9316-9.

[37] D. Hull, A unified approach to progressive crushing of fibre-reinforced composite tubes, Compos. Sci. Technol. 40 (1991) 377–421, https://doi.org/10.1016/0266-3538(91)90031-J.

[38] S.T. Pinho, P.P. Camanho, M.F. De Moura, Numerical simulation of the crushing process of composite materials, Int. J. Crashworthin. 9 (2004) 263–276, https://doi.org/10.1533/ijcr.2004.0287.

[39] M.J. Laffan, S.T. Pinho, P. Robinson, L. Iannucci, Measurement of the in situ ply fracture toughness associated with mode I fibre tensile failure in FRP. Part I: Data reduction, Compos. Sci. Technol. 70 (2010) 606–613, https://doi.org/10.1016/J.COMPSCITECH.2009.12.016.

[40] S.T. Pinho, P. Robinson, L. Iannucci, Fracture toughness of the tensile and compressive fibre failure modes in laminated composites, Compos. Sci. Technol. 66 (2006) 2069–2079, https://doi.org/10.1016/J.COMPSCITECH.2005.12.023.